Supplementary Information (SI) for Journal of Materials Chemistry C.

Elucidating Thermally Activated Luminescence Quenching in Eu^{III} β-Diketonate Complexes as Crystals or Polymeric Films for Application in Thermometry

Felipe S. M. Canisares,‡[a] Matheus G. Laurindo,‡[a] Leonardo F. Saraiva,[b,c] João H. A. Neto,[a] Javier A. Ellena,[c] Hermi F. Brito,[a] Airton G. Bispo-Jr[a]*

[a] Department of Fundamental Chemistry, Institute of Chemistry, University of São Paulo (USP), São Paulo, São Paulo 05508-000, Brazil.

[b] São Paulo State University (UNESP), School of Science and Technology, São Paulo, SP, Brazil.

[c] Institute of Inorganic Chemistry, Heinrich-Heine University Düsseldorf, 40225 Düsseldorf, NRW, Germany.

[d] São Carlos Institute of Physics, University of São Paulo, IFSC – USP, 13566-590, São Carlos, SP, Brazil.

‡ These authors contributed equally to this work.

* airton.bispo.junior@iq.usp.br

Contents

Supplementary note S1 – Synthesis and characterization

Preparation of the dinuclear Eu^{III} complex [$Eu_2(bpm)(nta)_6$]

$EuCl_3$ was first obtained by dissolving europium oxide (Eu_2O_3) in HCl in stoichiometric proportion (water as solvent), followed by drying to obtain $EuCl_3 \cdot 6H_2O$ as powder. For the synthesis, the ligand 4,4,4-Trifluoro-1-(2-naphthyl)-1,3-butanedione (nta, 1.9 mmol) was solubilized in 10 mL of methanol. 1.90 mmol of sodium hydroxide was added to deprotonate the ligand. In another vial, the bridge ligand 2,2'-bipyrimidine (bpm, 0.31 mmol) was solubilized in 10 mL of methanol and mixed with $EuCl_3 \cdot 6H_2O$ (0.62 mmol) solubilized in 10 mL of methanol. The deprotonated nta$^-$ ligand was slowly added in the bpm-Eu^{III} solution and the resulting mixture was refluxed for 4 h at 60 °C. The solution was filtered and allowed to evaporate. After one week, needle-like single crystals were obtained. A scheme of the synthesis is represented in Figure S1.

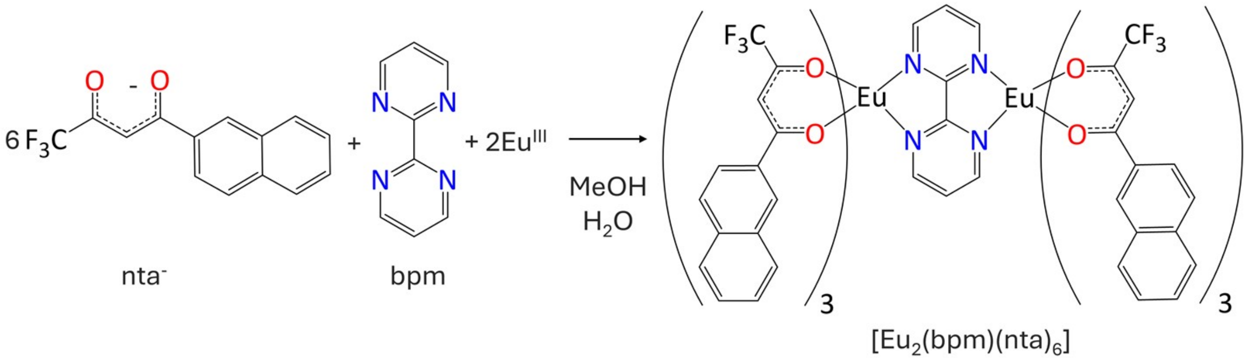

Figure S1. Schematic representation of the [$Eu_2(bpm)(nta)_6$] complex synthesis.

[$Eu_2(bpm)(nta)_6$]: FTIR (ATR cm^{-1}): 605 (m), 681 (m), 715 (w), 743 (m), 757 (w), 769 (m), 791 (s), 821 (w), 864 (w), 918 (m), 936 (m), 955 (m), 996 (w), 1018 (w), 1069 (m), 1112 (s), 1122 (s), 1133 (s), 1165 (m), 1187 (m), 1217 (m), 1252 (m), 1286 (s), 1356 (w), 1364 (w), 1389 (w), 1412 (w), 1456 (m), 1505 (s), 1527 (s), 1563 (s), 1558 (s), 1609 (s), 1637 (w), 1591 (s), 1619 (w), 2111 (w), 3062 (w). Anal. Calc.: C, 53.81; H, 2.65; N, 2.73; %. Found: C, 53.79; H, 2.92, N, 2.97.

Fabrication of the PMMA films

Poly(methyl) methacrylate (PMMA) films doped with the complex [$Eu_2(bpm)(nta)_6$] were prepared according to the procedure described in the literature.[1] The concentration of complex in the film was changed as 1, 5, 10, and 20wt.% relative to the PMMA mass. The compositions of the films are detailed in Table S1. PMMA was dissolved in acetone and after that, the complex was added at varying weight percentages. This solution was drop-casted onto a 5 × 5 cm^2 glass substrate and dried in a acetone-saturated atmosphere to prevent the formation of opaque films (Figure S2).

Table S1. Composition of the films.

Name	**PMMA**		**[Eu_2(bpm)(nta)$_6$]**	
	Wt.%	**Mass / g**	**Wt.%**	**Mass / g**
PMMA	100%	0.3000	-	-
PMMA:1%Eu^{III}	99%	0.2970	1%	0.0030
PMMA:5%Eu^{III}	95%	0.2850	5%	0.0150
PMMA:10%Eu^{III}	90%	0.2700	10%	0.0300
PMMA:20%Eu^{III}	80%	0.2400	20%	0.0600

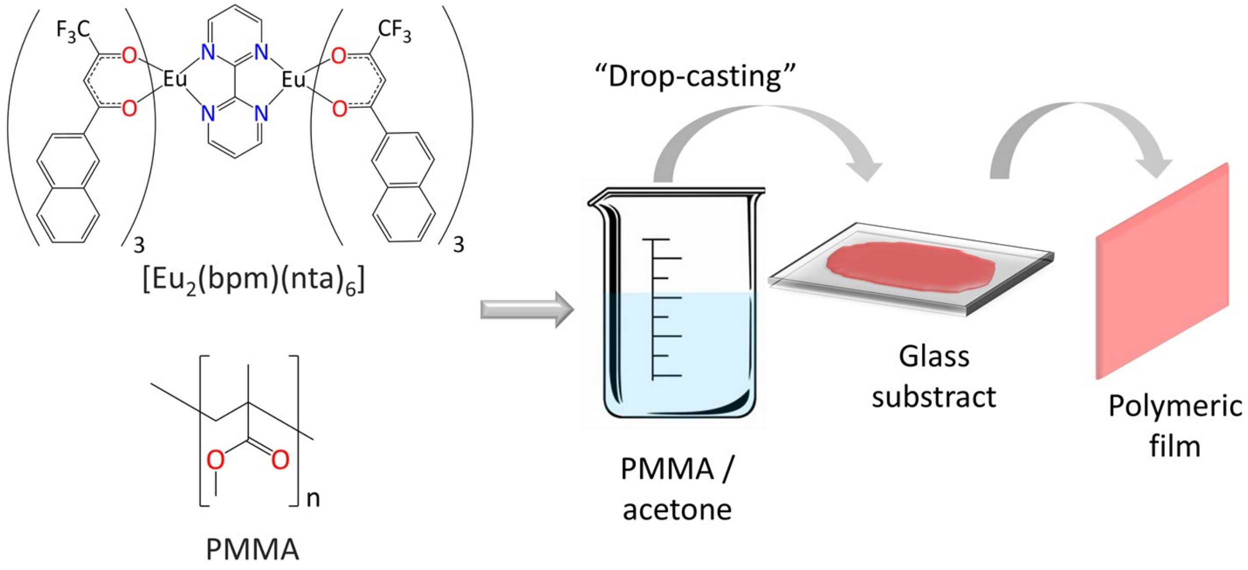

Figure S2. Synthesis of the PMMA films.

Characterization

Single-crystal X-Ray diffraction (SC-XRD). SC-XRD data collection of the [Eu_2(bpm)(nta)$_6$] complex was performed employing the Rigaku XtaLAB Synergy-S diffractometer, equipped with the HyPix-6000HE detector and MoK$_\alpha$ radiation (λ = 0.71073 Å at 100 K) microfocus with a sealed X-ray source. The crystals were selected and mounted in cryoloop with mineral oil. The collection strategies and cell refinement were carried out using the CrysAlisPro. The crystal structure was solved by direct methods employing SHELXLT XT (version 2014/4) and refined using SHELX 64.[2] A multi-scan absorption correction was performed. The CIF file was deposited in the Cambridge Structural Database with CCDC number of 2534491. Copies of the data can be accessed, free of charge, via www.ccdc.ac.uk.

Elemental analysis (CHN). CHN elemental analyses were performed using a PerkinElmer 2400 Series II at the Analytical Center of the Institute of Chemistry, University of São Paulo (USP), São Paulo, Brazil.

Fourier-transform infrared spectroscopy (FTIR). FTIR spectra were obtained using a Perkin Elmer spectrometer of Frontier model, equipped with ATR diamond. The measurements were undertaken from 4000 cm^{-1} to 400 cm^{-1}, with 2 cm^{-1} of resolution and 120 scans.

Thermogravimetry (TG). Thermogravimetry of the complexes was performed in a TGA Q500 V20.13, from 25 °C to 950 °C, with a heating rate of 10 °C min^{-1}, and an atmosphere of air (40 mL min^{-1})/N_2 (60 mL min^{-1}).

Diffuse reflectance spectroscopy (DRS) and transmittance spectra: DRS and transmittance spectra were recorded using a Shimadzu UV-2600 spectrometer equipped with solid-state and liquid sample holders. The solid-state integrating sphere is coated with $BaSO_4$, which also serves as reference for DRS measurements. Transmittance spectra were obtained using the liquid sample holder, with the films mounted perpendicular (90°) to the optical path. Air was used as reference for transmittance measurements. In both DRS and transmittance modes, the spectral resolution was set to 1 nm.

Room Temperature Photoluminescence (**PL**). PL were carried out in a Fluorolog-3 spectrofluorometer (Horiba FL3-22-iHR320) with double-gratings (1,200 grooves mm^{-1}, 330 nm blaze) in the excitation monochromator and double-gratings (1200 grooves mm^{-1}, 500 nm blaze) in the emission monochromator. An ozone-free xenon lamp of 450 W (Ushio) was used as a radiation source. A 150 W pulsed xenon lamp was used for time-resolved measurements by using a time-correlated single-photon counting (TCSPC) system. A photomultiplier (Hamamatsu R928P) operating at 950 V was used to collect the spectra in the ultraviolet and visible spectral regions, which were corrected according to the optical system of the emission monochromator and the photomultiplier response. The emission and excitation spectra were carried using the front face mode at 22.51°. The excitation and emission slits were kept in a position to lead to a spectral bandpass of 1 nm in all experiments.

Temperature-dependent photoluminescence (**PL**): Emission spectra from 77 K to 480 K were measured in the previously mentioned Fluorolog 3 equipment. The excitation and emission slits were kept in a position to lead to a spectral bandpass of 1 nm in all experiments (integration time of 0.1 s). To control the temperature, a Linkam accessory (THMS600), with an optical fiber set (NA = 0.22 - Horiba-FL-3000/FM4-3000) was used.

Absolute emission quantum yield. Photoluminescence quantum yield (PLQY) was measured in a Quanta Phi-2 integrating sphere coupled to the previously mentioned fluorimeter. For reference, the empty sphere coated with Spectralon (reflectance > 95%) was used.

Supplementary note S2 – Data analysis

Photophysical properties of Eu^{III}. The radiative decay rate (A_{rad}) of the Eu^{III} $^5D_0$ level was calculated from equations S1 and S2, where A is the Einstein coefficient of spontaneous emission. In equation S1, the term $I_{0\text{-}\lambda}$ is the area under the curve related to the $^5D_0 \rightarrow {}^7F_\lambda$ transition, $h\nu_{0-\lambda}$ is the energetic barycenter of the 0–λ transition, and $A_{01} = 14.65\ n^3$ in s^{-1}, where n is the refractive index (complex = 1.5, PMMA = 1.490[3]). The non-radiative decay rate (A_{nrad}) of the Eu^{III} $^5D_0$ level was calculated from equation S3, where τ is the $^5D_0$ level lifetime. Finally, the intrinsic Eu^{III} emission quantum yield (Q_{Eu}^{Eu}) was determined from equation S4. The average lifetime was calculated from equation S5, where the term A_i is the pre-exponential factor, or amplitude associate of each lifetime (τ_i) values.[4]

$$A_{0-\lambda} = A_{01}\frac{I_{0-\lambda}h\nu_{0-1}}{I_{0-1}h\nu_{0-\lambda}} \quad (S1)$$

$$A_{rad} = \sum_J A_{0-J} \quad (S2)$$

$$A_{total} = \frac{1}{\langle\tau\rangle} = A_{rad} + A_{nrad} \quad (S3)$$

$$Q_{Eu}^{Eu} = \frac{A_{rad}}{A_{rad} + A_{nrad}} \quad (S4)$$

$$\langle\tau\rangle = \frac{\sum A_i\tau_i^2}{\sum A_i\tau_i} \quad (S5)$$

The experimental Judd-Ofelt intensity parameters were calculated from equation S6, where $|\langle {}^7F_J \| U^{(\lambda)} \| {}^5D_0 \rangle|^2$ represents the square reduced matrix element,s which values are equal to 0.0032 for Ω_2 and 0.0023 for Ω_4; h is the Planck's constant, e is the electron charge, c is the speed of light in vacuum, ω *is the* angular frequency of the incident radiation field, ε_0 is vacuum permittivity constants, and X is the Lorentz local field correction equal to $n(n^2+2)^2/9$.[5]

$$\Omega_\lambda = \frac{3hc^3A_{0\lambda}}{8\pi e^2\omega^3\chi|\langle {}^7F_J \| U^{(\lambda)} \| {}^5D_0 \rangle|^2} \quad (S6)$$

Luminescence thermometry. The relative thermal sensitivity of the complexes was calculated from equation S7, where Δ is the thermometric parameter and T is the temperature. The temperature uncertainty (δT) is calculated by equation S8, where $\delta\Delta/\Delta$ is the relative uncertainty in the determination of the $^5D_0$ lifetime, which was considered as at about 0.001 ms.[6]

$$S_r = \frac{1}{\Delta}\left|\frac{d\Delta}{dT}\right| \quad (S7)$$

$$\delta T = \frac{1}{S_r}\frac{\delta\Delta}{\Delta} \quad (S8)$$

Supplementary note S3 – Computational protocol

All electronic structure calculations within the density functional theory (DFT) and time dependent (TD-DFT) level of theory discussed in the main text and Supporting Information were carried out with the quantum chemistry package Orca 6.0.1.[7,8]

Geometry Optimization. In the present work, only the position of the hydrogen atoms was optimized via DFT with the PBE0 functional[9] along with the D4 dispersion correction[10]. During the optimization, the Def2-TZVP basis set[11] was used with no auxiliary resolution of identity (RI) approximation.

Excited-States calculation. With the optimized structure obtained from the previous step, a TD-DFT calculation was performed to obtain the singlets and triplets excited states, and its composition in terms of molecular orbitals. For this purpose, the range-separated ωB97x hybrid functional[12] with the D4 dispersion correction as well[10]. All atoms in the system were described with the same Def2-TZVP basis set, except Eu^{III}, which was described by the Stuttgart-Cologne adapted MWB52 effective core potential (ECP) along with its Gaussian-type basis set.[13] This ECP is widely employed for such calculations, as they allow us to consider the systems' multiplicity as a singlet due to the buried nature of the 4*f* orbitals.[14] It should be noticed that by switching from Eu^{III} to other Ln^{III} the employed ECP should change as well, as each ECP is specific for each Ln^{III}. The general method is written as ωB97x-D4/Def2-TZVP/MWB52. To consider the film, we employed the same strategy described in reference [15], in which the polymeric medium was described as a static environment by including the refractive index and dielectric constant of poly(methyl) methacrylate. This approximation is well-suited due to the low concentration of the complex dispersed into the polymer matrix: 1 wt.% used for the thermally dependent essays.

Intramolecular energy transfer

With the TD-DFT results the rates of intramolecular energy transfer (IET) from the excited state (S_1 and T_1) of the ligand to Eu^{III} were calculated. The calculation considered three main mechanisms, the dipole-dipole (W_{d-d}), dipole-multipole (W_{m-d}), and exchange mechanism (W_{ex}), as written in Equation S9 – 11[16,17,18]. In this case, the overall rates are obtained as a sum between each mechanism, i.e., $W = W_{d-d} + W_{m-d} + W_{ex}$.

$$W_{d-d} = \frac{S_L(1-\sigma_1)^2 4\pi e^2}{(2J+1)G\ \hbar\ R_L^6}\sum_{\lambda}\Omega_{\lambda}^{FED}\langle\psi'J'\,||U^{(\lambda)}||\,\psi J\rangle^2 F \tag{S9}$$

$$W_{m-d} = \frac{S_L\quad 2\pi e^2}{(2J+1)G\ \hbar}\sum_{\lambda}(\lambda+1)\frac{\langle r^{\lambda}\rangle^2}{\left(R_L^{\lambda+2}\right)^2}\langle f\,||C^{(\lambda)}||\,f\rangle^2 \times (1-\sigma_1)^2\langle\psi'J'\,||U^{(\lambda)}||\,\psi J\rangle^2 F \tag{S10}$$

$$W_{ex} = \frac{(1-\sigma_0)^2\, 8\pi e^2}{(2J+1)G\ \hbar\ R_L^4}\langle\psi'J'\,||S||\,\psi J\rangle^2\sum_{m}\left\langle\phi\,\middle|\left|\sum_{j}\mu_z(j)s_m(j)\right|\middle|\,\phi^*\right\rangle^2 F \tag{S11}$$

In all equations, R_L represents the distance between the donor and acceptor states, which is obtained from the excited state calculation (Equation S12). It is noteworthy that R_L considers the individual distance between the atomic center and the Ln^{III}. In this case, c_i is the i-th atomic orbital coefficient included in the ligand donor excited states (S_1 or T_1), $R_L(i)$ is the distance between the c_i center to the Ln^{III}, and a_j is the weight of the j-th orbital that composes the excited state.[19]

$$R_L = \frac{\sum_{i,j} a_j^2 c_i^2 R_L(i)}{\sum_{i,j} a_j^2 c_i^2} \tag{S12}$$

It should be noted that only the FED contribution is considered (Equation S13), since in Kushida's expressions, the appearance of Ω_λ is due to opposite parity mixing.[20] The values of the squared reduced matrix elements, $\langle \psi' J' \| U^{(\lambda)} \| \psi J \rangle^2$, were taken from Carnall et al.[21] S_L represents the dipole strength of the ligand transition involved in the IET process, with values of 10^{-36} and 10^{-40} esu^2 cm^2 for S_1 and T_1, respectively[22]. $\langle r^\lambda \rangle$ represents the 4*f* radial integrals, G the ligand degeneracy (G = 1 or 3 for S_1 or T_1, respectively). The reduced matrix elements of Racah's tensor operator are considered in Equation S10, $\langle f \| C^{(\lambda)} \| f \rangle$, as well as the shielding factors in Equation S9 - 11, $(1 - \sigma_k)$, which depends on the overlap integrals between valence orbitals of the pair Ln-O[23,24]. In the exchange expression, s_m is the spin operator in the ligand and μ_z is the dipole operator (its z-component).[17] The $\langle \psi' J' \| S \| \psi J \rangle$ represents the reduced matrix elements of the spin operator, which were calculated using free ion wavefunctions in the intermediate coupling scheme.

It is worth noting that the IET is non-resonant. In this sense, an energy mismatch (F) condition between donor and acceptor states is needed, taken the form of Equation S13 and S14 for the ligand-to-metal energy transfer.

$$F = \frac{G(\delta,T)}{\hbar\gamma_L} \sqrt{\frac{\ln(2)}{\pi}} e^{-\left(\frac{\delta}{\hbar\gamma_L}\right)^2 \ln(2)} \tag{S13}$$

$$G(\delta,T) = \begin{cases} 1 \; if \; \delta \geq 0 \\ \exp\left(\frac{\delta}{k_B T}\right) if \; \delta < 0 \end{cases} \tag{S14}$$

In this expression, δ represents the energy difference between donor and acceptor states, γ_L is the bandwidth at half-height of the donor state, assumed here to have a typical value of 3000 cm^{-1} for S_1 and T_1 states.[22] A special case is when $\delta < 0$ because the energy mismatch factor is multiplied by the Boltzmann factor, where k_B is the Boltzmann constant, with value of 0.695 cm^{-1} K^{-1} and T the temperature.

Multiphonon relaxation.

Multiphonon relaxation (MPR) arises from the cooperative coupling of multiple lattice phonons that assist an electronic transition, with its probability governed by the ratio between the electronic energy gap (ΔE) and the effective phonon energy ($\hbar\omega$).[25] Larger phonon energies increase the probability of nonradiative decay, as fewer phonons are required to bridge a given energy gap. This concept constitutes the basis of the energy gap law, which can be described by Equation S15[26,27], where α is a host-specific parameter and p the number of phonons necessary to bridge the gap.

$$W \propto exp(- \alpha p) \tag{S15}$$

If the offset between the representative harmonic potentials of the vibronic states is close to zero, the multiphonon relaxation can be expressed in terms of Equation S16.[28] In this equation, 1 account for the spontaneous emission contribution of the effective vibrational modes, whereas $W_{nr}(0)$ denotes the limiting spontaneous non-radiative rate at 0 K, g_1 the degeneracy factor associated with the level ($g_1 = 2J + 1$) and $\langle n_k \rangle$ represents the thermal average occupation number of any phonon mode with quasi-momentum $\hbar k$, given by Equation S17.

$$W_{MPR} = g_1 W_{nr}(0) \prod_k \left(1 + \langle n_k \rangle\right)^p \tag{S16}$$

$$\langle n_k \rangle = \left(exp\left(\frac{\hbar\omega_k}{k_B T} \right) - 1 \right)^{-1} \tag{S17}$$

In this study, the phonon energy was taken as the phonon cutoff (maximum energy), obtained from the FTIR measurements depicted in Figure 2F.

Supplementary note S4 – Additional crystallographic data

Table S2. Crystallographic data of [Eu_2(bpm)(nta)$_6$].

	[Eu_2(bpm)(nta)$_6$]
CCDC deposition number	2534491
Empirical formula	$C_{92}H_{54}Eu_2F_{18}N_4O_{12}$
Molecular weight, g mol^{-1}	2053.37
Temperature, K	100
Wavelength, Å	1.54184
Crystal system	Triclinic
Space group	$P\bar{1}$
a, Å	9.9805(2)
b, Å	12.6721(2)
c, Å	17.2729(3)
α, °	106.234(2)
β, °	97.168(2)
γ, °	101.980(2)
Volume	2012.54(7)
No. of formula units/unit cell, Z	1
Density (*ρ*), g cm^{-3} calc'd.	1.694
Absorption coefficient (μ) mm^{-1}	11.959
F(0 0 0)	1006.6
Crystal size, mm^3	0.22 × 0.15 × 0.07
Minimum and maximum transmittance	0.337,1.000
Theta range, °	9.24 - 140.16
Index ranges (h k l)	(12 16 21)
No. of reflections measured	45131
No. of independent reflections	7641
R(int)	0.0392
Completeness, %	0.997
Data / restraints / parameters	7641/0/602
R1, wR^2 (I > 2 σ(I))^a	0.0235, 0.0570
R1, wR^2 (all data)	0.0243, 0.0574
Goodness of fit on F^2	1.046
Largest differential peak and hole, e$^-$/Å^3	0.54/-0.49

Table S3. Intramolecular and intermolecular Eu ··· Eu distances (Å) in [Eu_2(bpm)(nta)$_6$].

Distance / Å	**d / Å**
Intramolecular Eu ··· Eu distance	6.8236(5)
Intermolecular Eu ··· Eudistance	9.1142(6)

Table S4. Shape analysis of the Eu^{III} polyhedron of [Eu_2(bpm)$(nta)_6$] using SHAPE 2.1.[29] Values in the table are the continuous shape measures (CShM, dimensionless) for each idealized geometry.

Idealized geometry	Short name	Point group	
Triangular dodecahedron	**TDD-8**	$\boldsymbol{D_{2d}}$	**0.502**
Square antiprism	SAPR-8	D_{4d}	1.927
Biaugmented trigonal prism	BTPR-8	C_{2v}	2.105
Biaugmented trigonal prism J50	JBTPR-8	C_{2v}	2.644
Snub diphenoid J84	JSD-8	D_{2d}	3.274
Cube	CU-8	Oh	8.922
Triakis tetrahedron	TT-8	Td	9.694
Johnson gyrobifastigium J26	JGBF-8	D_{2d}	14.916
Hexagonal bipyramid	HBPY-8	D_{6h}	15.454
Heptagonal pyramid	HPY-8	C_{7v}	23.377
Elongated trigonal bipyramid	ETBPY-8	D_{3h}	24.278
Johnson elongated triangular bipyramid J14	JETBPY-8	D_{3h}	29.556
Octagon	OP-8	D_{8h}	32.326

Table S5. Bite angles (°) of ligands in [Eu_2(bpm)$(nta)_6$].

Bond	Angle / °
N1 – Eu – N2	62.703(58)
O1a – Eu – O2a	71.465(56)
O1b – Eu – O2b	71.680(55)
O1c – Eu – O2c	71.912(59)

Table S6. Eu – N and Eu – O bond distances (Å) in the first coordination sphere of [Eu_2(bpm)$(nta)_6$].

Bond	Distances / Å
Eu – N1	2.5970(2)
Eu – N2	2.6114(18)
Eu – O1a	2.2498(18)
Eu – O2a	2.3547(14)
Eu – O1b	2.3672(17)
Eu – O2b	2.3446(15)
Eu – O1c	2.3527(19)
Eu – O2c	2.3060(15)

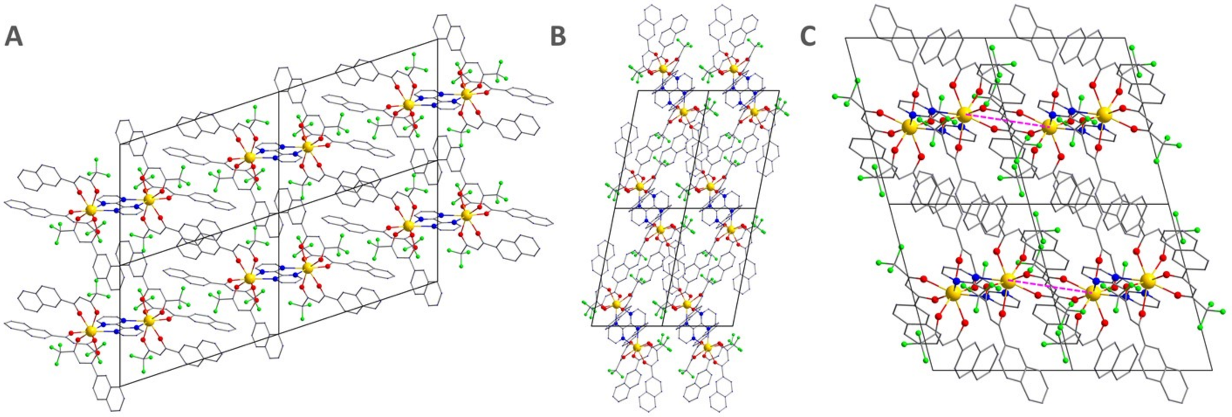

Figure S3. View of the packing arrangement along the crystallographic (a) *a*, (b) *b*, and (c) c-axis in [Eu_2(bpm)(nta)$_6$]. Pink dashed lines represent the shortest Eu · · · Eu intermolecular distance (9.1142 Å). Carbon = gray, fluorine = green, nitrogen = blue, europium = yellow. Hydrogen atoms have been omitted for the sake of clarity.

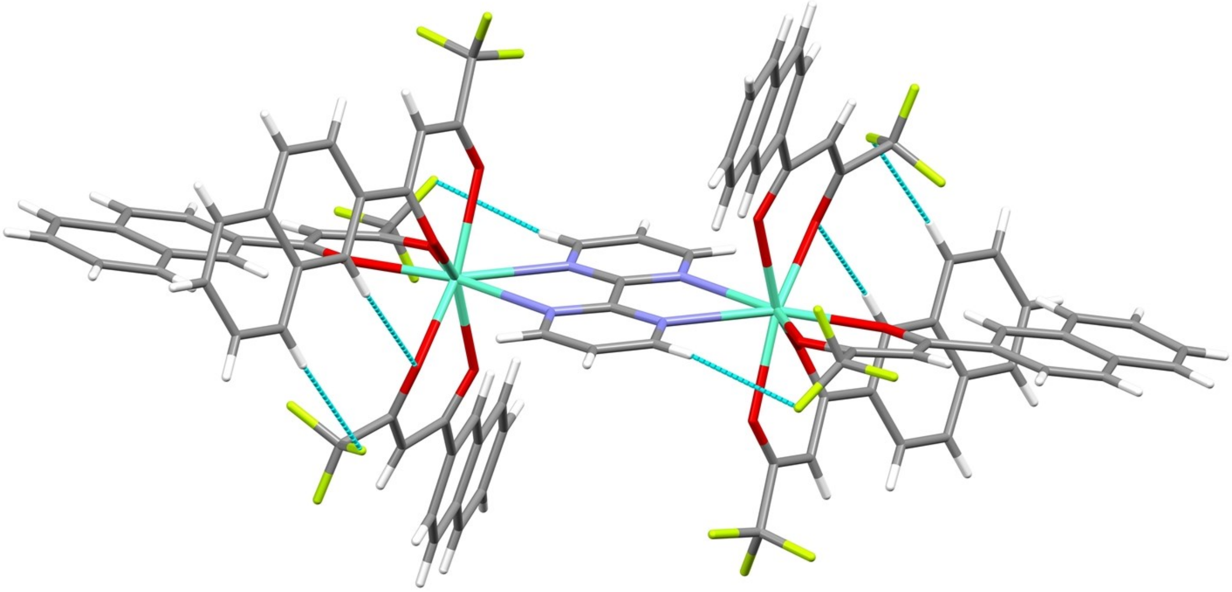

Figure S4. Representation of the intramolecular H-bonds (dashed blue lines) in [Eu_2(bpm)(nta)$_6$]. Carbon = gray, hydrogen = white, fluorine = yellow, nitrogen = violet, europium = cyan.

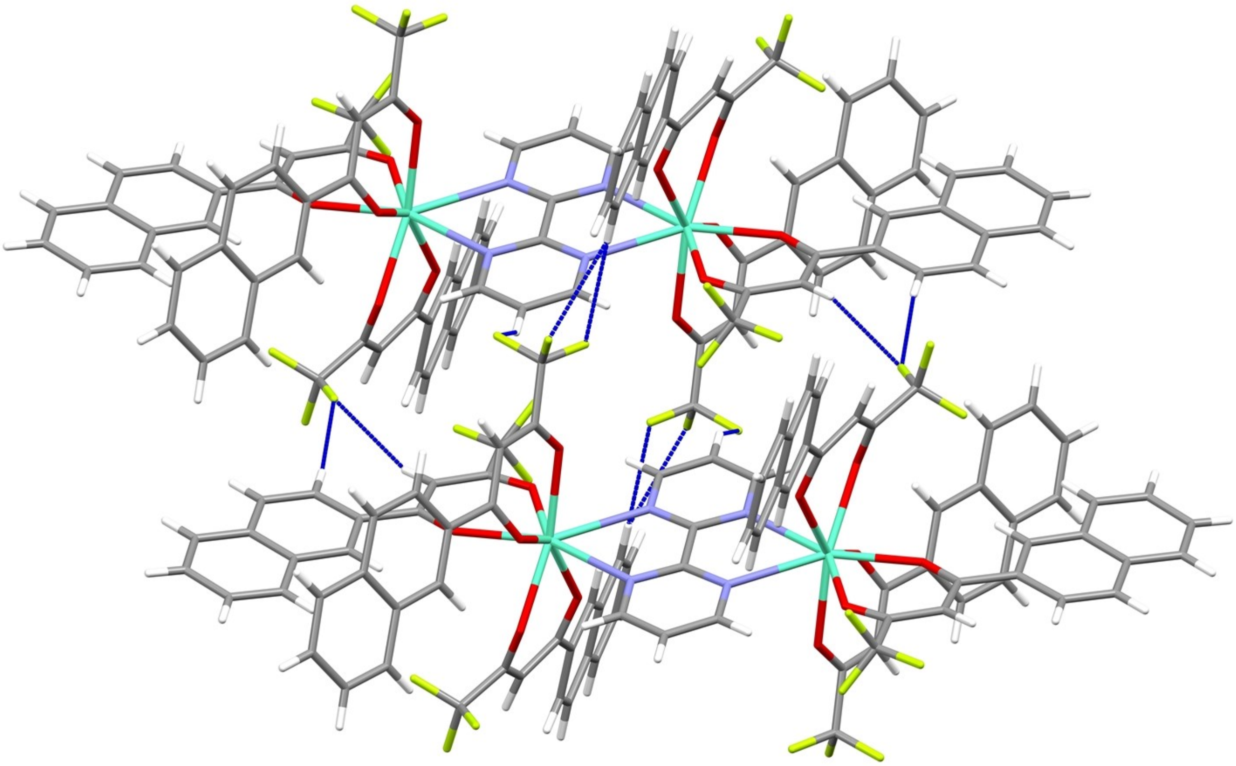

Figure S5. Representation of the intermolecular H-bonds (dashed blue lines) in [Eu_2(bpm)(nta)$_6$]. Carbon = gray, hydrogen = white, fluorine =yellow, nitrogen = violet, europium = cyan.

Table S7. Intermolecular and intramolecular H-bond distances (Å) in [Eu_2(bpm)(nta)$_6$].

Intramolecular H-bond / Å		Intermolecular H-bond / Å	
F2A···H8B	3.256	**F2A···H3C**	2.588
F2C···H4	3.073	**F2A···H14C**	2.411
O1A···H6B	3.209	**H3···F1B**	2.506
		F2B···H8A	2.913
		F3B···H8A	2.814

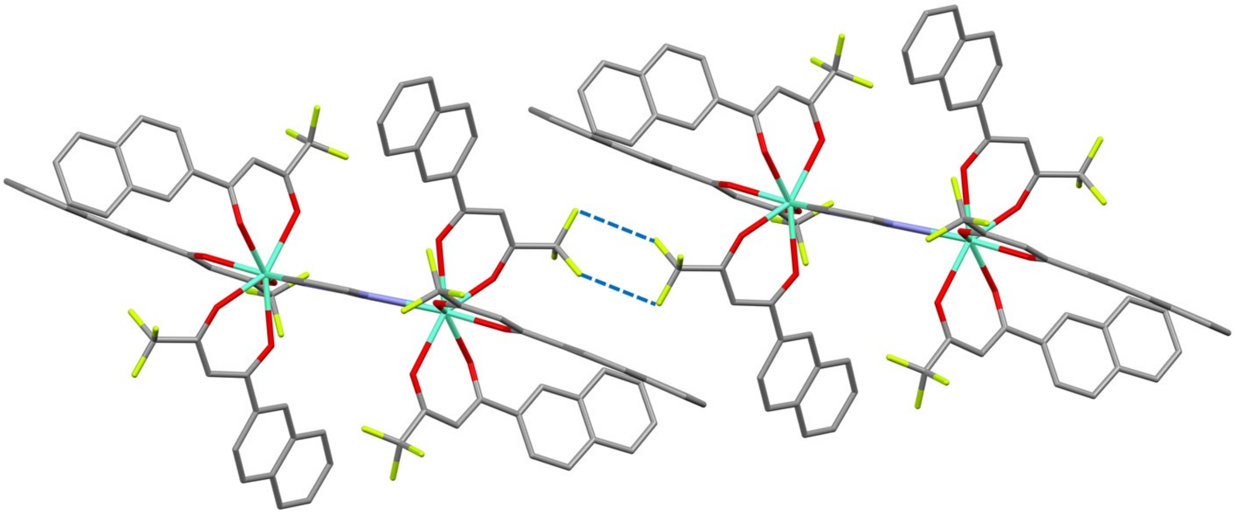

Figure S6. Intermolecular F···F contacts (blue dashed lines) in [Eu_2(bpm)(nta)$_6$]. The F···F contact has distance of 2.937 Å and angle of 125.98 **°.**

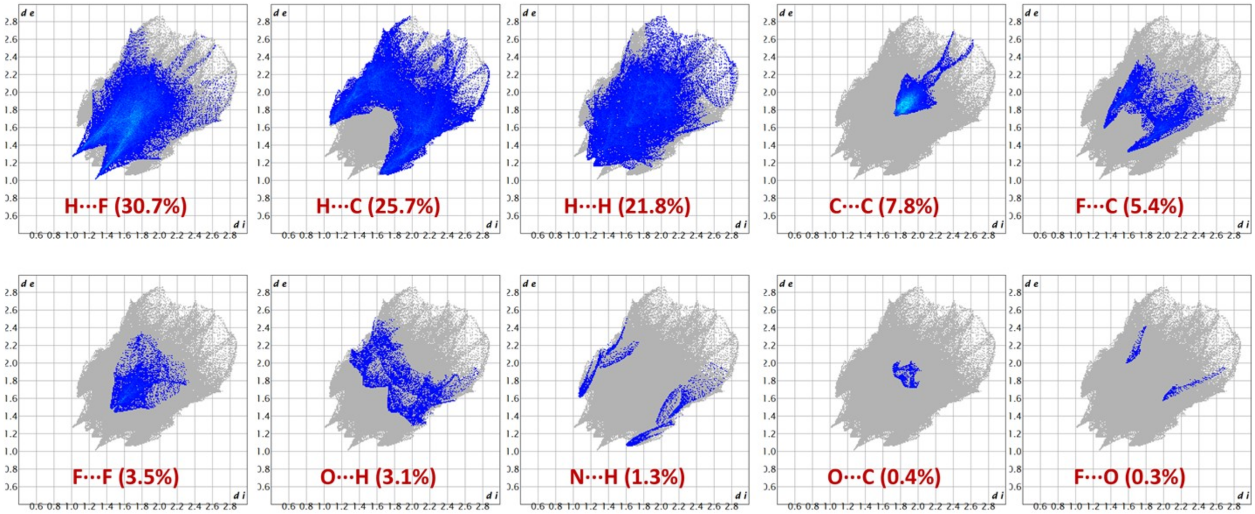

Figure S7. The 2D fingerprint plots of interatomic interactions of [Eu_2(bpm)(nta)$_6$], showing the percentages of contacts contributed to the total Hirshfeld surface area of the molecules.

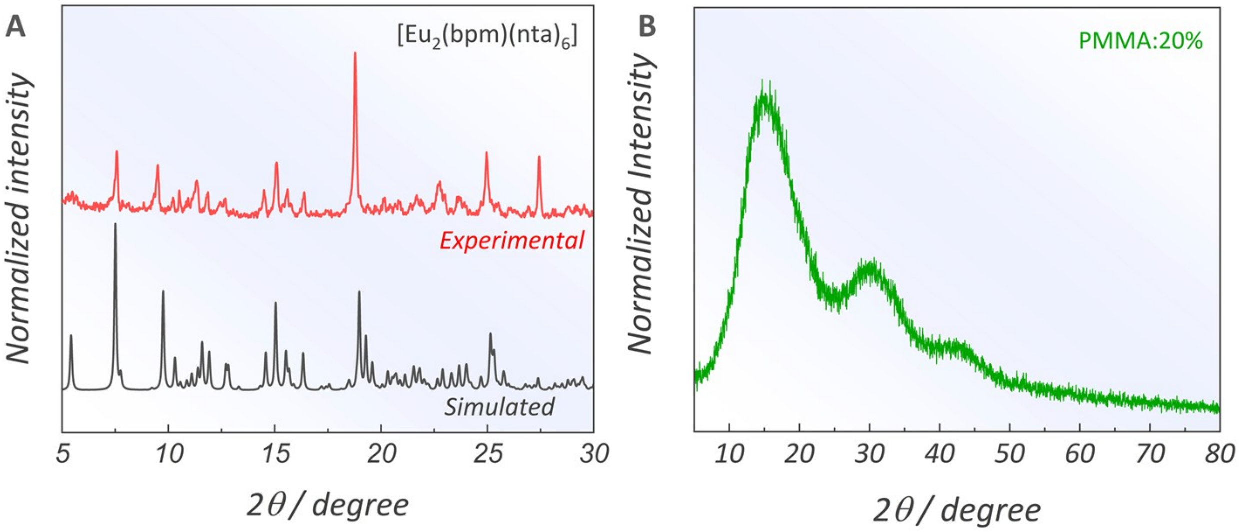

Figure S8. (a) Powder XRD of crashed crystals of [Eu$_2$(bpm)(nta)$_6$] compared to the simulated patter determined from the SC-XRD measurements. (b) Powder XRD collected for the PMMA:20% film. In (a), the experimental PXRD pattern agrees with that simulated from SC-XRD. Although the crystals were ground prior to measurement, their needle-like morphology promotes preferential growth along a specific crystallographic direction and can induce preferred orientation in the sample holder, affecting the relative peak intensities. Moreover, the PXRD was collected at 300 K while SC-XRD was measured at 100 K, which accounts for slight changes in the peak position.[30] In (b), for the PMMA:20% film with higher concentration of [Eu$_2$(bpm)(nta)$_6$], no diffraction peaks assigned to the complex were observed; only the amorphous halo characteristic of PMMA.

Supplementary note S5 – Thermogravimetry

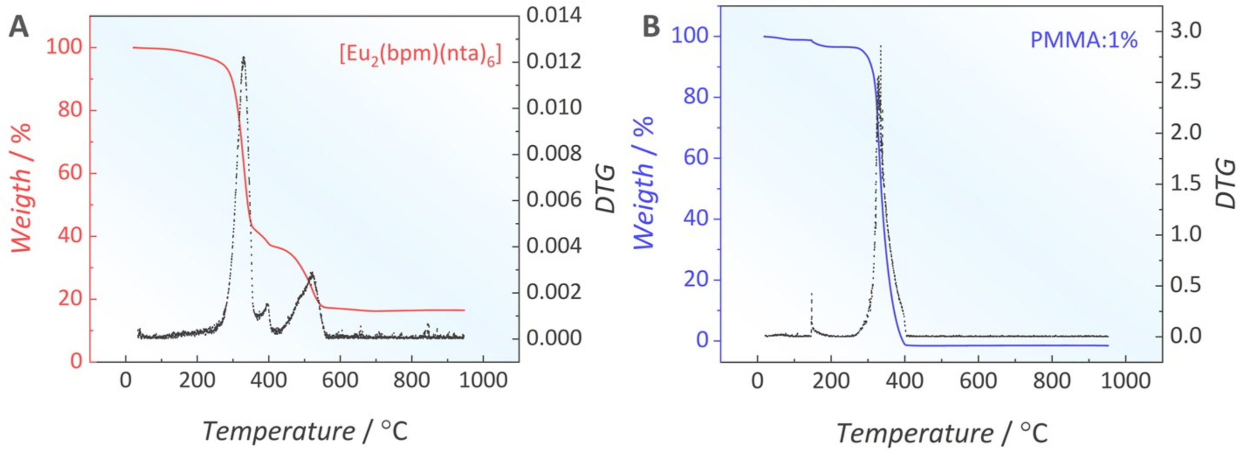

Figure S9. Thermogravimetry and derivate of thermogravimetry (DTG) measured for the (a) [Eu_2(bpm)(nta)$_6$] complex as crystals and (b) PMMA:1% film.

Supplementary note S6 – Structural characterization of the films

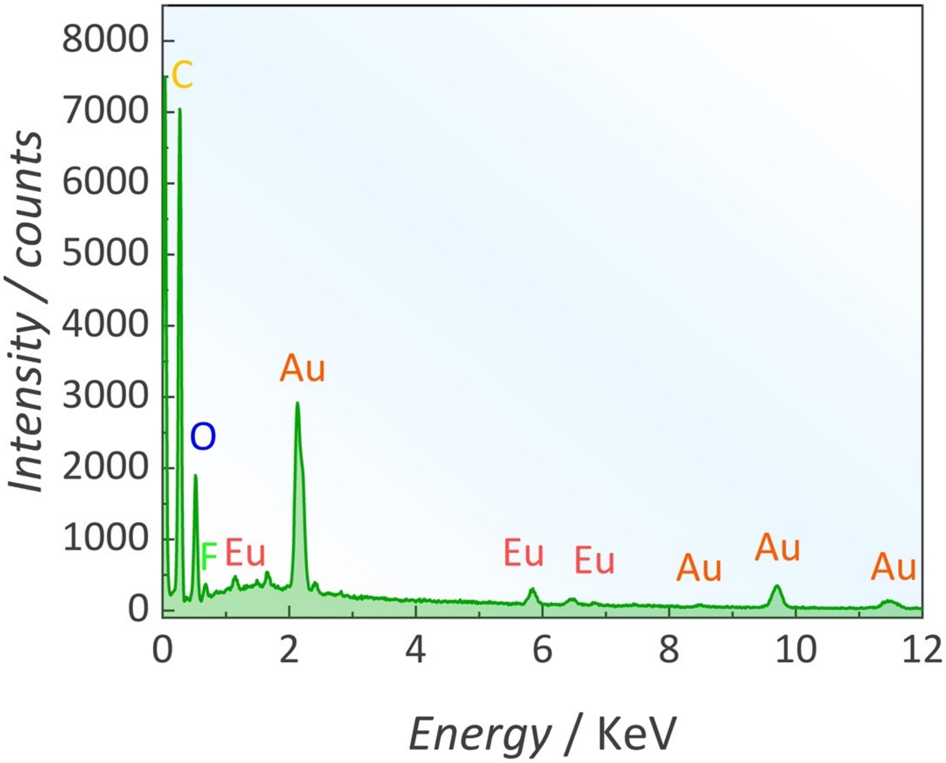

Figure S10. Energy dispersive spectroscopy (EDS) of the (a) PMMA:10% film highlighting the assignments of the detected chemical elements. The PMMA:10% film was chosen due to its larger amount of complex, favouring the detection of europium in the measurement.

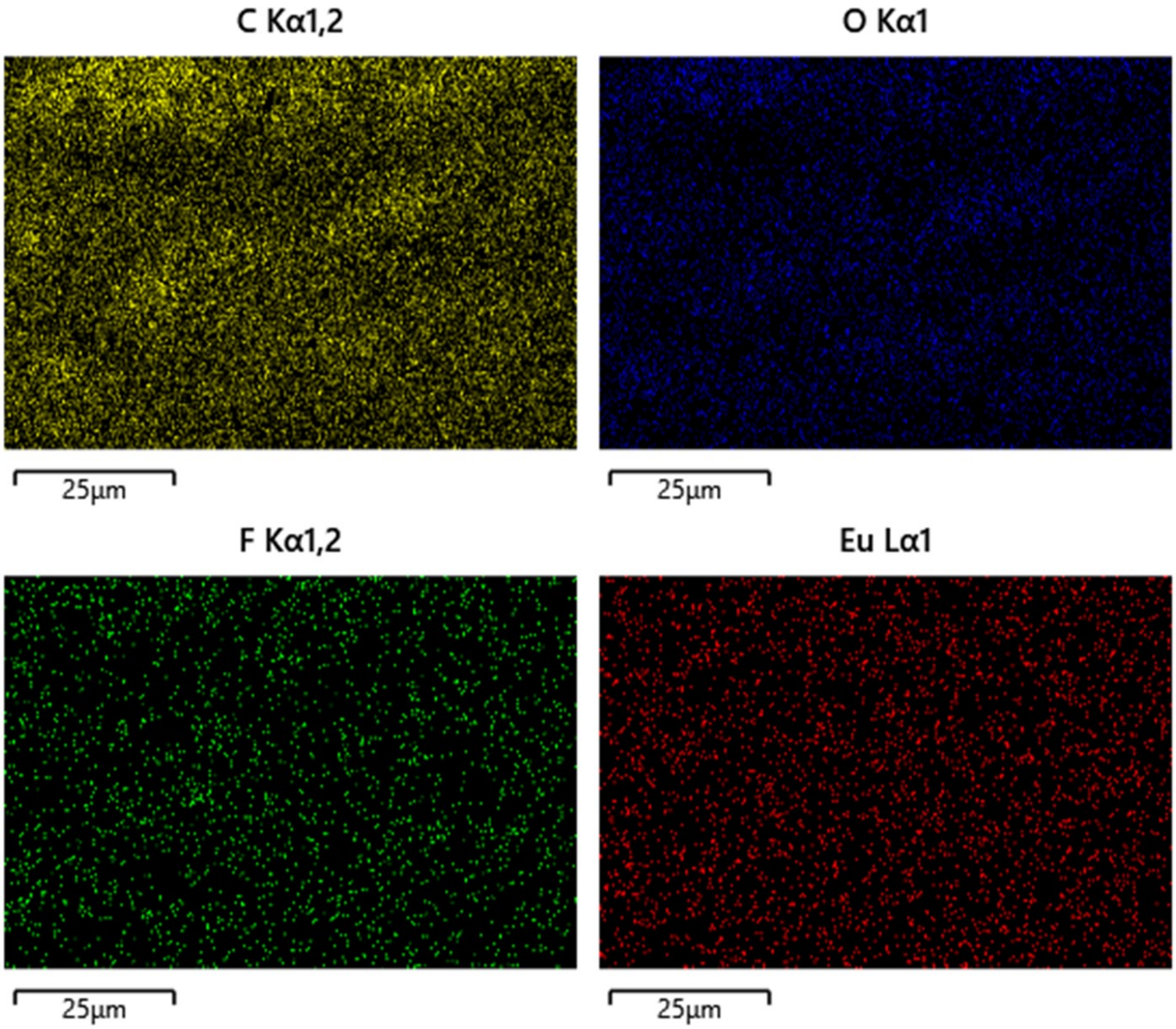

Figure S11. Chemical mapping of the PMMA:10% film highlighting the elemental maps of Carbon, Oxygen, Fluorine, and Europium.

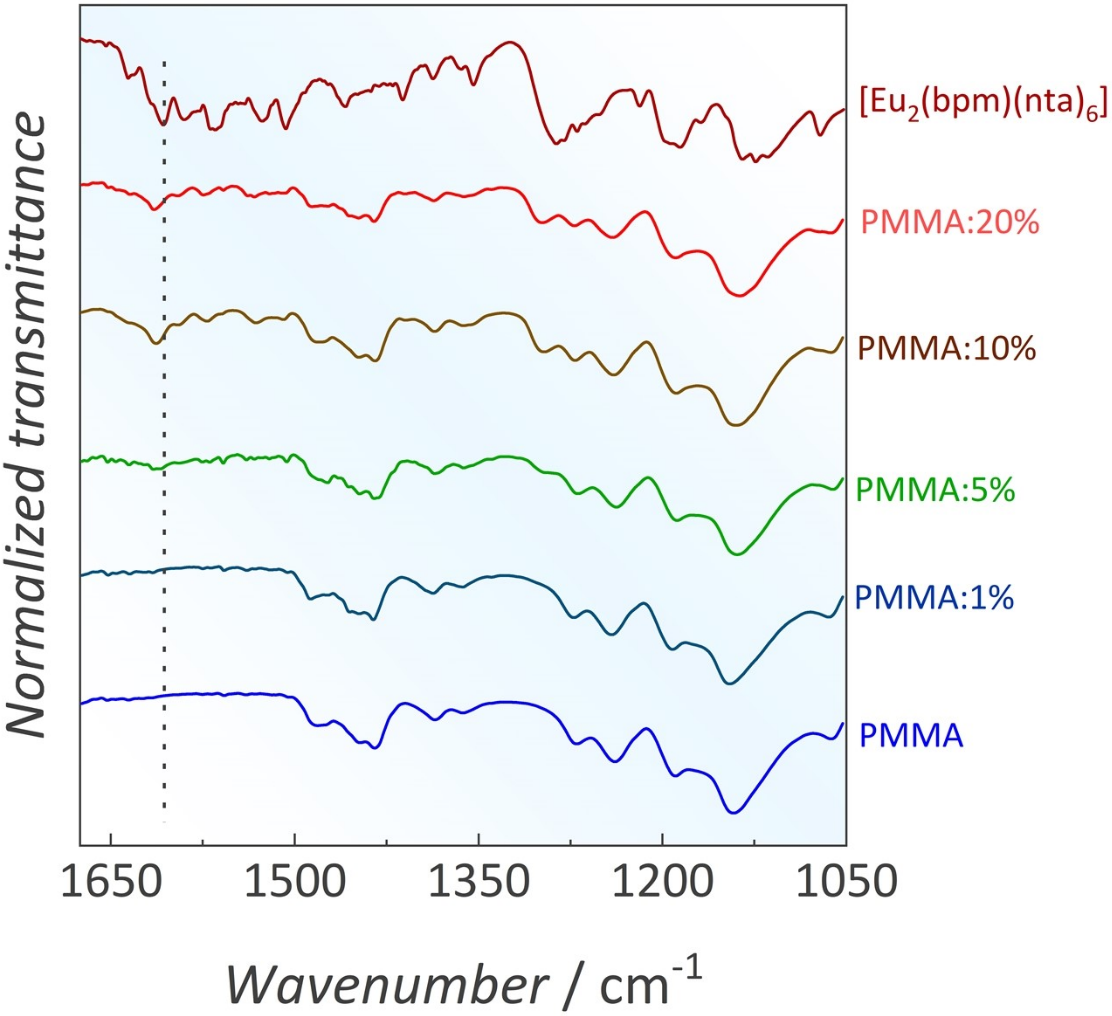

Figure S12. Magnification of the FTIR of the PMMA:X% films compared with that of the [Eu_2(bpm)(nta)$_6$] complex, highlighting the shift of the band assigned to the ν(C=O) vibrational mode of the complex.

Supplementary note S7 – Photoluminescence data at room temperature

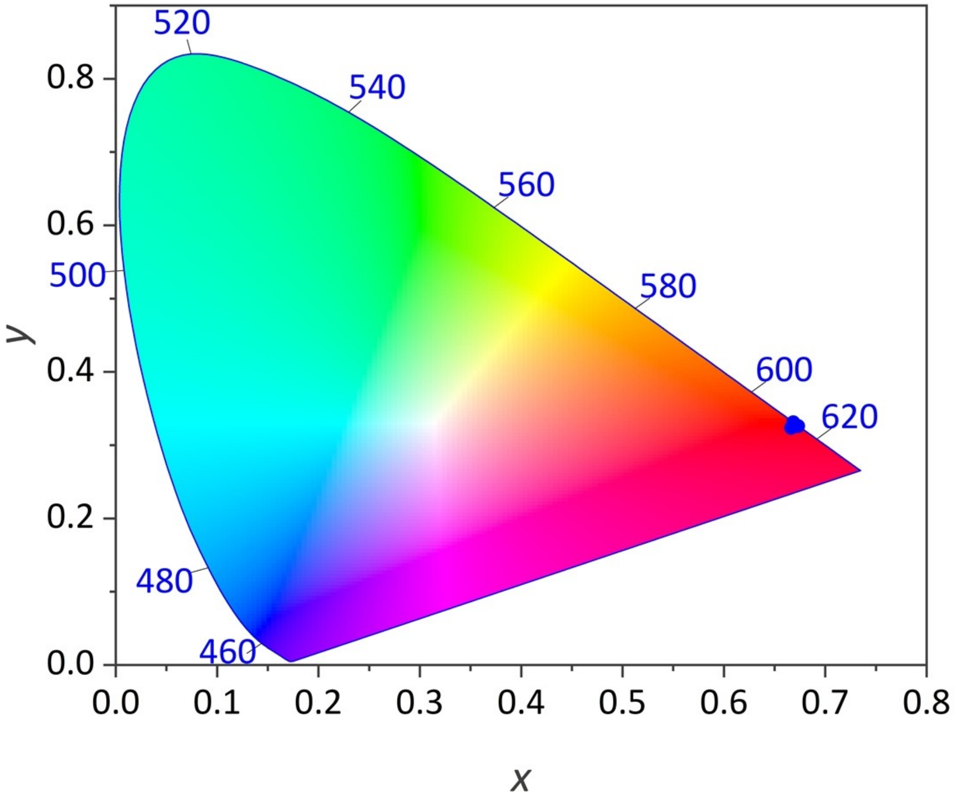

Figure S13. 1931 *Commission Internationale d'Eclairage* (CIE) color diagrams illustrating the emission color coordinates of the [Eu_2(bpm)(nta)$_6$] complex as crystal and dispersed in PMMA. The points are overlapped in the diagram.

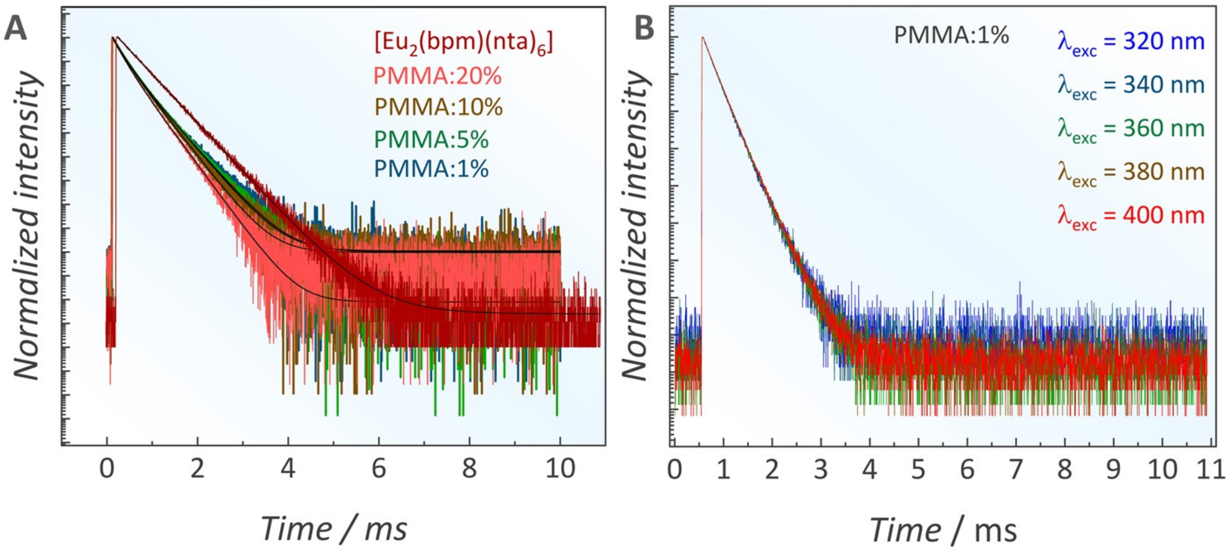

Figure S14. (a) Emission decay curves (300 K) monitored at λ_{exc} = 380 nm and λ_{em} = 613 nm to determine the Eu^{III} $^5D_0$ level lifetime. The black lines represent the fitting to a monoexponential ([Eu_2(bpm)$(nta)_6$]) or biexponential (PMMA films) decay function ($R^2 > 0.9$). (b) Emission decay curves (300 K) monitoring the Eu^{III} $^5D_0 \rightarrow {}^7F_2$ transition at 613 nm and different excitation wavelength (λ_{exc} = 320 – 400 nm) for the PMMA:1% film.

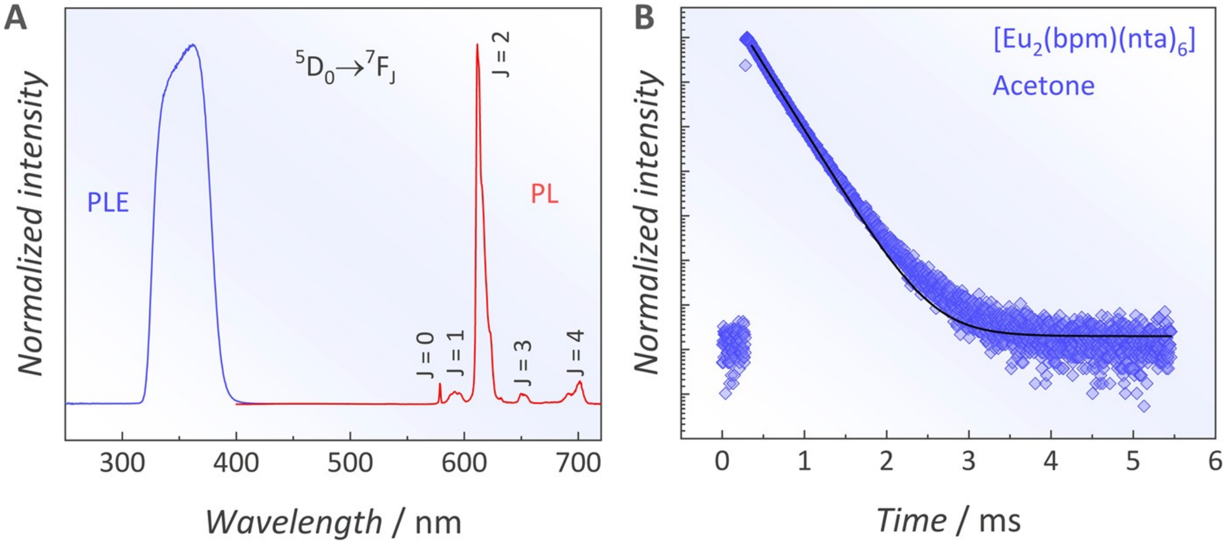

Figure S15. (a) Excitation (PLE, λ_{em}= 613 nm) and emission (PL, λ_{ex}= 365 nm) spectra of [Eu_2(bpm)$(nta)_6$] in acetone solution (5.2 10^{-5} mol L^{-1}). (b) Emission decay curves (300 K) of [Eu_2(bpm)$(nta)_6$] in acetone solution (5.2 10^{-5} mol L^{-1}) monitored at (a) λ_{exc} = 365 nm, λ_{em} = 613 nm. The curve was fitted according to a monoexponential decay function (black line), with R^2 = 0.99.

Supplementary note S8 – Temperature-dependent photoluminescence

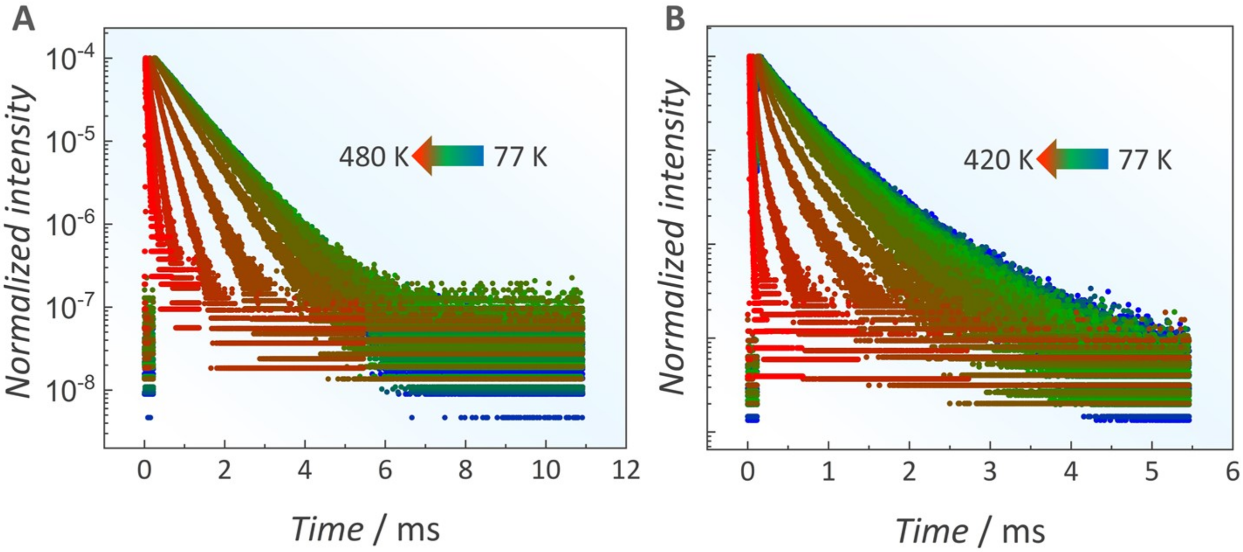

Figure S16. Emission decay curves (λ_{exc} = 380 nm and λ_{em} = 613 nm) dependent on the temperature for (a) the [Eu_2(bpm)(nta)$_6$] crystal (77 – 480 K) and (b) PMMA:1% film (77 – 420 K).

Supplementary note S9 – Calculations of the luminescence dynamics

Table S8. Theoretical Judd-Ofelt intensity parameters (10^{-20} cm^2) compared to the experimental values for the $[Eu_2(bpm)(nta)_6]$ complex as crystals or in PMMA film.

	Ω_2^{exp}	Ω_2^{theo}	Ω_4^{exp}	Ω_4^{theo}	Ω_6^{exp}	Ω_6^{theo}
$[Eu_2(bpm)(nta)_6]$	23.38	22.01	6.03	8.24	–	1.60
Film	29.90	28.22	7.86	7.95	–	1.34

Table S9. Singlet (S_1) and triplet (T_1) state energies calculated via the method described in the computational procedure (supplementary note S3), as well as the distance between the centroid donor and the acceptor (Eu^{III}).

	Parameters			
	$E(S_1)$ / cm^{-1}	**R_L (S_1) / Å**	**$E(T_1)$ / cm^{-1}**	**R_L (T_1) / Å**
$[Eu_2(bpm)(nta)_6]$	25149	3.41	21301	3.63
Film	22558	3.41	21245	3.41

Table S10. Forward and total backward IET rates (in units of s^{-1}) for the [Eu$_2$(bpm)(nta)$_6$] complex as crystals calculated at 300 K. W^S and W^T are the total energy transfer via S$_1$ and T$_1$ states.

Pathway	**Donor**	**Acceptor**	**δ / cm^{-1}**	W	W_{BET}
6	$S_1\rightarrow S_0$	$^7F_0\rightarrow{}^5D_0$	7856	8.674×10^{5}	4.521×10^{-11}
7	$S_1\rightarrow S_0$	$^7F_0\rightarrow{}^5D_1$	6122	1.431×10^{9}	1.017×10^{-4}
8	$S_1\rightarrow S_0$	$^7F_0\rightarrow{}^5D_2$	3666	0.000×10^{0}	0.000×10^{0}
9	$S_1\rightarrow S_0$	$^7F_0\rightarrow{}^5D_3$	794	0.000×10^{0}	0.000×10^{0}
10	$S_1\rightarrow S_0$	$^7F_0\rightarrow{}^5L_6$	-176	2.790×10^{6}	5.999×10^{5}
11	$S_1\rightarrow S_0$	$^7F_0\rightarrow{}^5L_7$	-1208	0.000×10^{0}	0.000×10^{0}
12	$S_1\rightarrow S_0$	$^7F_0\rightarrow{}^5G_2$	-1243	0.000×10^{0}	0.000×10^{0}
13	$S_1\rightarrow S_0$	$^7F_0\rightarrow{}^5G_3$	-1473	0.000×10^{0}	0.000×10^{0}
14	$S_1\rightarrow S_0$	$^7F_0\rightarrow{}^5G_4$	-1586	0.000×10^{0}	0.000×10^{0}
15	$S_1\rightarrow S_0$	$^7F_0\rightarrow{}^5G_6$	-1603	5.915×10^{2}	1.193×10^{5}
16	$S_1\rightarrow S_0$	$^7F_0\rightarrow{}^5G_5$	-1614	0.000×10^{0}	0.000×10^{0}
17	$S_1\rightarrow S_0$	$^7F_0\rightarrow{}^5L_8$	-2095	0.000×10^{0}	0.000×10^{0}
18	$S_1\rightarrow S_0$	$^7F_0\rightarrow{}^5D_4$	-2437	3.349×10^{1}	5.326×10^{5}
19	$S_1\rightarrow S_0$	$^7F_0\rightarrow{}^5L_9$	-2811	0.000×10^{0}	0.000×10^{0}
20	$S_1\rightarrow S_0$	$^7F_0\rightarrow{}^5L_{10}$	-3278	0.000×10^{0}	0.000×10^{0}
26	$S_1\rightarrow S_0$	$^7F_1\rightarrow{}^5D_0$	8228	4.025×10^{7}	5.237×10^{-9}
27	$S_1\rightarrow S_0$	$^7F_1\rightarrow{}^5D_1$	6494	6.643×10^{6}	1.178×10^{-6}
28	$S_1\rightarrow S_0$	$^7F_1\rightarrow{}^5D_2$	4038	8.251×10^{7}	0.000×10^{0}
29	$S_1\rightarrow S_0$	$^7F_1\rightarrow{}^5D_3$	1166	2.480×10^{7}	2.358×10^{5}
30	$S_1\rightarrow S_0$	$^7F_1\rightarrow{}^5L_6$	196	2.595×10^{5}	1.393×10^{5}
31	$S_1\rightarrow S_0$	$^7F_1\rightarrow{}^5L_7$	-836	8.902×10^{3}	5.842×10^{5}
32	$S_1\rightarrow S_0$	$^7F_1\rightarrow{}^5G_2$	-871	1.171×10^{7}	$2.728e\times10^{9}$
33	$S_1\rightarrow S_0$	$^7F_1\rightarrow{}^5G_3$	-1101	6.491×10^{4}	$3.253e\times10^{7}$
34	$S_1\rightarrow S_0$	$^7F_1\rightarrow{}^5G_4$	-1214	0.000×10^{0}	0.000×10^{0}
35	$S_1\rightarrow S_0$	$^7F_1\rightarrow{}^5G_6$	-1231	3.404×10^{2}	1.714×10^{5}
36	$S_1\rightarrow S_0$	$^7F_1\rightarrow{}^5G_5$	-1242	9.922×10^{2}	6.224×10^{5}
37	$S_1\rightarrow S_0$	$^7F_1\rightarrow{}^5L_8$	-1723	0.000×10^{0}	0.000×10^{0}
38	$S_1\rightarrow S_0$	$^7F_1\rightarrow{}^5D_4$	-2065	0.000×10^{0}	0.000×10^{0}
39	$S_1\rightarrow S_0$	$^7F_1\rightarrow{}^5L_9$	-2439	0.000×10^{0}	0.000×10^{0}
40	$S_1\rightarrow S_0$	$^7F_1\rightarrow{}^5L_{10}$	-2906	0.000×10^{0}	0.000×10^{0}
	W^S	**1.601×10^{9} s^{-1}**	W^S_{BET}	**2.736×10^{9} s^{-1}**	
6	$T_1\rightarrow S_0$	$^7F_0\rightarrow{}^5D_0$	4008	2.887×10^{9}	3.182×10^{-6}
7	$T_1\rightarrow S_0$	$^7F_0\rightarrow{}^5D_1$	2274	0.000×10^{0}	2.122×10^{4}
8	$T_1\rightarrow S_0$	$^7F_0\rightarrow{}^5D_2$	-182	0.000×10^{0}	0.000×10^{0}
9	$T_1\rightarrow S_0$	$^7F_0\rightarrow{}^5D_3$	-3054	1.533×10^{-7}	0.000×10^{0}

10	$T_1 \rightarrow S_0$	$^7F_0 \rightarrow {}^5L_6$	-4024	0.000×10^{0}	3.410×10^{0}
11	$T_1 \rightarrow S_0$	$^7F_0 \rightarrow {}^5L_7$	-5056	0.000×10^{0}	0.000×10^{0}
12	$T_1 \rightarrow S_0$	$^7F_0 \rightarrow {}^5G_2$	-5091	0.000×10^{0}	0.000×10^{0}
13	$T_1 \rightarrow S_0$	$^7F_0 \rightarrow {}^5G_3$	-5321	0.000×10^{0}	0.000×10^{0}
14	$T_1 \rightarrow S_0$	$^7F_0 \rightarrow {}^5G_4$	-5434	1.395×10^{-11}	0.000×10^{0}
15	$T_1 \rightarrow S_0$	$^7F_0 \rightarrow {}^5G_6$	-5451	0.000×10^{0}	2.911×10^{-1}
16	$T_1 \rightarrow S_0$	$^7F_0 \rightarrow {}^5G_5$	-5462	0.000×10^{0}	0.000×10^{0}
17	$T_1 \rightarrow S_0$	$^7F_0 \rightarrow {}^5L_8$	-5943	3.890×10^{-13}	0.000×10^{0}
18	$T_1 \rightarrow S_0$	$^7F_0 \rightarrow {}^5D_4$	-6285	0.000×10^{0}	6.401×10^{-1}
19	$T_1 \rightarrow S_0$	$^7F_0 \rightarrow {}^5L_9$	-6659	0.000×10^{0}	0.000×10^{0}
20	$T_1 \rightarrow S_0$	$^7F_0 \rightarrow {}^5L_{10}$	-7126	0.000×10^{0}	0.000×10^{0}
26	$T_1 \rightarrow S_0$	$^7F_1 \rightarrow {}^5D_0$	4380	2.83×10^{8}	3.809×10^{0}
27	$T_1 \rightarrow S_0$	$^7F_1 \rightarrow {}^5D_1$	2646	1.76×10^{5}	3.223×10^{0}
28	$T_1 \rightarrow S_0$	$^7F_1 \rightarrow {}^5D_2$	190	4.84×10^{7}	6.952×10^{7}
29	$T_1 \rightarrow S_0$	$^7F_1 \rightarrow {}^5D_3$	-2682	8.26×10^{-4}	8.132×10^{2}
30	$T_1 \rightarrow S_0$	$^7F_1 \rightarrow {}^5L_6$	-3652	4.55×10^{8}	2.527×10^{0}
31	$T_1 \rightarrow S_0$	$^7F_1 \rightarrow {}^5L_7$	-4684	3.31×10^{-10}	2.246×10^{0}
32	$T_1 \rightarrow S_0$	$^7F_1 \rightarrow {}^5G_2$	-4719	3.62×10^{-3}	8.720×10^{7}
33	$T_1 \rightarrow S_0$	$^7F_1 \rightarrow {}^5G_3$	-4949	2.10×10^{-9}	1.087×10^{2}
34	$T_1 \rightarrow S_0$	$^7F_1 \rightarrow {}^5G_4$	-5062	0.00×10^{-3}	0.000×10^{0}
35	$T_1 \rightarrow S_0$	$^7F_1 \rightarrow {}^5G_6$	-5079	1.00×10^{-11}	5.213×10^{-1}
36	$T_1 \rightarrow S_0$	$^7F_1 \rightarrow {}^5G_5$	-5090	2.70×10^{-11}	1.752×10^{0}
37	$T_1 \rightarrow S_0$	$^7F_1 \rightarrow {}^5L_8$	-5571	0.00×10^{3}	0.000×10^{0}
38	$T_1 \rightarrow S_0$	$^7F_1 \rightarrow {}^5D_4$	-5913	0.00×10^{3}	0.000×10^{0}
39	$T_1 \rightarrow S_0$	$^7F_1 \rightarrow {}^5L_9$	-6287	0.00×10^{-3}	0.000×10^{0}
40	$T_1 \rightarrow S_0$	$^7F_1 \rightarrow {}^5L_{10}$	-6754	0.00×10^{-3}	0.000×10^{0}
	W^T	**3.219×10^{9} s^{-1}**	W_{BET}^{T}	**1.567×10^{8} s^{-1}**	

Table S11. Forward and total backward IET rates (in units of s^{-1}) calculated at 300 K for the $[Eu_2(bpm)(nta)_6]$ complex in PMMA. W^S and W^T are the total energy transfer via S_1 and T_1 states.

Pathway	**Donor**	**Acceptor**	**δ / cm^{-1}**	W	W_{BET}
6	$S_1 \rightarrow S_0$	$^7F_0 \rightarrow {}^5D_0$	5265	1.189×10^{7}	1.545×10^{-4}
7	$S_1 \rightarrow S_0$	$^7F_0 \rightarrow {}^5D_1$	3531	$9.823e\times10^{9}$	1.740×10^{2}
8	$S_1 \rightarrow S_0$	$^7F_0 \rightarrow {}^5D_2$	1075	0.000×10^{0}	0.000×10^{0}
9	$S_1 \rightarrow S_0$	$^7F_0 \rightarrow {}^5D_3$	-1797	0.000×10^{0}	0.000×10^{0}
10	$S_1 \rightarrow S_0$	$^7F_0 \rightarrow {}^5L_6$	-2767	6.221×10^{0}	3.334×10^{5}
11	$S_1 \rightarrow S_0$	$^7F_0 \rightarrow {}^5L_7$	-3799	0.000×10^{0}	0.000×10^{0}
12	$S_1 \rightarrow S_0$	$^7F_0 \rightarrow {}^5G_2$	-3834	0.000×10^{0}	0.000×10^{0}
13	$S_1 \rightarrow S_0$	$^7F_0 \rightarrow {}^5G_3$	-4064	0.000×10^{0}	0.000×10^{0}
14	$S_1 \rightarrow S_0$	$^7F_0 \rightarrow {}^5G_4$	-4177	0.000×10^{0}	0.000×10^{0}
15	$S_1 \rightarrow S_0$	$^7F_0 \rightarrow {}^5G_6$	-4194	7.463×10^{-4}	3.752×10^{4}
16	$S_1 \rightarrow S_0$	$^7F_0 \rightarrow {}^5G_5$	-4205	0.000×10^{0}	0.000×10^{0}
17	$S_1 \rightarrow S_0$	$^7F_0 \rightarrow {}^5L_8$	-4686	0.000×10^{0}	0.000×10^{0}
18	$S_1 \rightarrow S_0$	$^7F_0 \rightarrow {}^5D_4$	-5028	3.029×10^{-5}	1.201×105
19	$S_1 \rightarrow S_0$	$^7F_0 \rightarrow {}^5L_9$	-5402	0.000×10^{0}	0.000×10^{0}
20	$S_1 \rightarrow S_0$	$^7F_0 \rightarrow {}^5L_{10}$	-5869	0.000×10^{0}	0.000×10^{0}
26	$S_1 \rightarrow S_0$	$^7F_1 \rightarrow {}^5D_0$	5637	6.403×10^{8}	2.076×10^{-2}
27	$S_1 \rightarrow S_0$	$^7F_1 \rightarrow {}^5D_1$	3903	5.289×10^{7}	2.338×10^{0}
28	$S_1 \rightarrow S_0$	$^7F_1 \rightarrow {}^5D_2$	1447	2.465×10^{8}	8.530×10^{5}
29	$S_1 \rightarrow S_0$	$^7F_1 \rightarrow {}^5D_3$	-1425	2.534×10^{4}	6.009×10^{7}
30	$S_1 \rightarrow S_0$	$^7F_1 \rightarrow {}^5L_6$	-2395	1.719×10^{0}	2.299×10^{5}
31	$S_1 \rightarrow S_0$	$^7F_1 \rightarrow {}^5L_7$	-3427	1.525×10^{-2}	2.495×10^{5}
32	$S_1 \rightarrow S_0$	$^7F_1 \rightarrow {}^5G_2$	-3462	1.979×10^{1}	1.149×10^{9}
33	$S_1 \rightarrow S_0$	$^7F_1 \rightarrow {}^5G_3$	-3692	1.001×10^{-1}	1.250×10^{7}
34	$S_1 \rightarrow S_0$	$^7F_1 \rightarrow {}^5G_4$	-3805	0.000×10^{0}	0.000×10^{0}
35	$S_1 \rightarrow S_0$	$^7F_1 \rightarrow {}^5G_6$	-3822	4.982×10^{-4}	6.252×10^{4}
36	$S_1 \rightarrow S_0$	$^7F_1 \rightarrow {}^5G_5$	-3833	1.446×10^{-3}	2.261×10^{5}
37	$S_1 \rightarrow S_0$	$^7F_1 \rightarrow {}^5L_8$	-4314	0.000×10^{0}	0.000×10^{0}
38	$S_1 \rightarrow S_0$	$^7F_1 \rightarrow {}^5D_4$	-4656	0.000×10^{0}	0.000×10^{0}
39	$S_1 \rightarrow S_0$	$^7F_1 \rightarrow {}^5L_9$	-5030	0.000×10^{0}	0.000×10^{0}
40	$S_1 \rightarrow S_0$	$^7F_1 \rightarrow {}^5L_{10}$	-5497	0.000×10^{0}	0.000×10^{0}
	W^S	**1.077×10^{10} s^{-1}**	W^S_{BET}	**1.224×10^{9} s^{-1}**	
6	$T_1 \rightarrow S_0$	$^7F_0 \rightarrow {}^5D_0$	3952	1.007×10^{3}	7.103×10^{-6}
7	$T_1 \rightarrow S_0$	$^7F_0 \rightarrow {}^5D_1$	2218	5.856×10^{9}	5.631×10^{4}
8	$T_1 \rightarrow S_0$	$^7F_0 \rightarrow {}^5D_2$	-238	0.000×10^{0}	0.000×10^{0}
9	$T_1 \rightarrow S_0$	$^7F_0 \rightarrow {}^5D_3$	-3110	0.000×10^{0}	0.000×10^{0}
10	$T_1 \rightarrow S_0$	$^7F_0 \rightarrow {}^5L_6$	-4080	1.911×10^{-7}	5.562×10^{0}
11	$T_1 \rightarrow S_0$	$^7F_0 \rightarrow {}^5L_7$	-5112	0.000×10^{0}	0.000×10^{0}

12	$T_1 \rightarrow S_0$	$^7F_0 \rightarrow {}^5G_2$	-5147	0.000×10^0	0.000×10^0
13	$T_1 \rightarrow S_0$	$^7F_0 \rightarrow {}^5G_3$	-5377	0.000×10^0	0.000×10^0
14	$T_1 \rightarrow S_0$	$^7F_0 \rightarrow {}^5G_4$	-5490	0.000×10^0	0.000×10^0
15	$T_1 \rightarrow S_0$	$^7F_0 \rightarrow {}^5G_6$	-5507	1.718×10^{-11}	4.689×10^{-1}
16	$T_1 \rightarrow S_0$	$^7F_0 \rightarrow {}^5G_5$	-5518	0.000×10^0	0.000×10^0
17	$T_1 \rightarrow S_0$	$^7F_0 \rightarrow {}^5L_8$	-5999	0.000×10^0	0.000×10^0
18	$T_1 \rightarrow S_0$	$^7F_0 \rightarrow {}^5D_4$	-6341	5.890×10^{-13}	1.268×10^0
19	$T_1 \rightarrow S_0$	$^7F_0 \rightarrow {}^5L_9$	-6715	0.000×10^0	0.000×10^0
20	$T_1 \rightarrow S_0$	$^7F_0 \rightarrow {}^5L_{10}$	-7182	0.000×10^0	0.000×10^0
26	$T_1 \rightarrow S_0$	$^7F_1 \rightarrow {}^5D_0$	4324	5.844×10^8	1.029×10^1
27	$T_1 \rightarrow S_0$	$^7F_1 \rightarrow {}^5D_1$	2590	3.567×10^5	8.562×10^0
28	$T_1 \rightarrow S_0$	$^7F_1 \rightarrow {}^5D_2$	134	9.642×10^7	1.811×10^8
29	$T_1 \rightarrow S_0$	$^7F_1 \rightarrow {}^5D_3$	-2738	1.021×10^{-3}	1.315×10^3
30	$T_1 \rightarrow S_0$	$^7F_1 \rightarrow {}^5L_6$	-3708	5.692×10^{-8}	4.135×10^0
31	$T_1 \rightarrow S_0$	$^7F_1 \rightarrow {}^5L_7$	-4740	4.100×10^{-10}	3.642×10^0
32	$T_1 \rightarrow S_0$	$^7F_1 \rightarrow {}^5G_2$	-4775	5.283×10^{-3}	1.665×10^8
33	$T_1 \rightarrow S_0$	$^7F_1 \rightarrow {}^5G_3$	-5005	2.549×10^{-9}	1.729×10^2
34	$T_1 \rightarrow S_0$	$^7F_1 \rightarrow {}^5G_4$	-5118	0.000×10^0	0.000×10^0
35	$T_1 \rightarrow S_0$	$^7F_1 \rightarrow {}^5G_6$	-5135	1.236×10^{-11}	8.424×10^{-1}
36	$T_1 \rightarrow S_0$	$^7F_1 \rightarrow {}^5G_5$	-5146	3.580×10^{-11}	3.039×10^0
37	$T_1 \rightarrow S_0$	$^7F_1 \rightarrow {}^5L_8$	-5627	0.000×10^0	0.000×10^0
38	$T_1 \rightarrow S_0$	$^7F_1 \rightarrow {}^5D_4$	-5969	0.000×10^0	0.000×10^0
39	$T_1 \rightarrow S_0$	$^7F_1 \rightarrow {}^5L_9$	-6343	0.000×10^0	0.000×10^0
40	$T_1 \rightarrow S_0$	$^7F_1 \rightarrow {}^5L_{10}$	-6810	0.000×10^0	0.000×10^0
	W^T	**6.537×10^9 s^{-1}**	W_{BET}^T	**3.477×10^8 s^{-1}**	

Supplementary note S10 – Further thermometry data

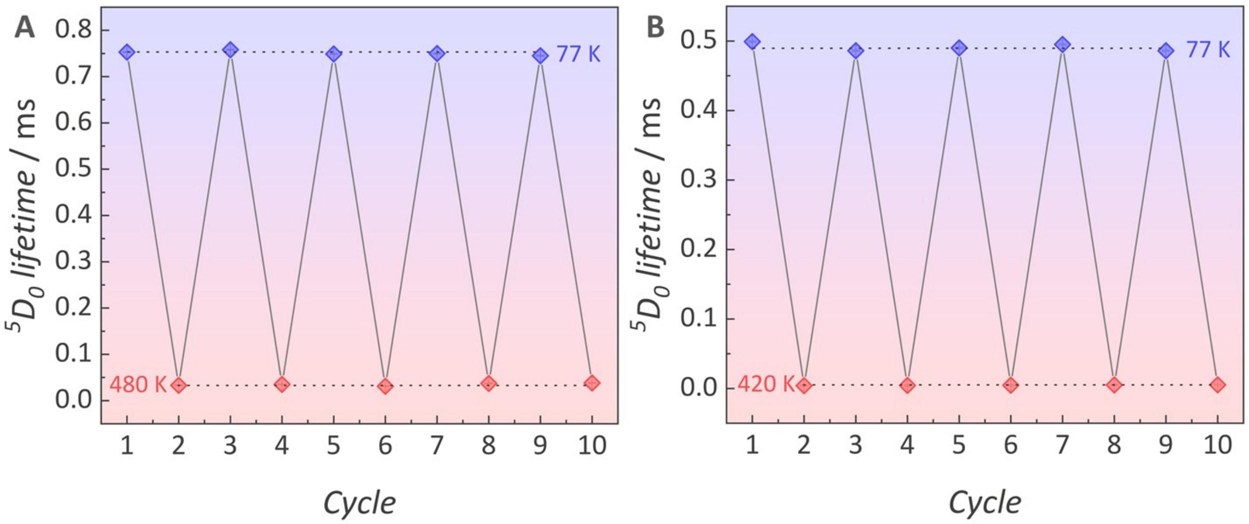

Figure S17. $^5D_0$ lifetime recorded in 10 heating–cooling temperature cycles for (a) $[Eu_2(bpm)(nta)_6]$ and (b) PMMA:1% film.

Supplementary note S11 – Derivations of temperature range and maximum sensitivity

(*i*) Maximum temperature range

We can start the derivations from Equation 3 of the main text:

$$S_r(T) = \frac{\Delta E \qquad g_1 A_{nrad}(0)e^{\left(-\Delta E/k_B T\right)}}{k_B T^2 \left(A_{rad} + g_1 A_{nrad}(0)e^{\left(-\Delta E/k_B T\right)}\right)}$$

By choosing a nominal value of sensitivity S_0, we set the condition that $S_r(T) > S_0$, leading to Equation S18.

$$\frac{\Delta E \qquad g_1 A_{nrad}(0)e^{\left(-\Delta E/k_B T\right)}}{k_B T^2 \left(A_{rad} + g_1 A_{nrad}(0)e^{\left(-\Delta E/k_B T\right)}\right)} > S_0 \tag{S18}$$

In this equation, we can define the temperature-induced non-radiative deactivation as: $A_{nrad}(T) = g_1 A_{nrad}(0)e^{\left(-\Delta E/k_B T\right)}$, in which we can plug into Equation S18, generating Eq S19.

$$\frac{\Delta E \qquad A_{nrad}(T)}{k_B T^2 \left(A_{rad} + A_{nrad}(T)\right)} > S_0 \Rightarrow \frac{A_{nrad}(T)}{\left(A_{rad} + A_{nrad}(T)\right)} > \frac{S_0 k_B T^2}{\Delta E} \tag{S19}$$

It is noteworthy that Equation S19 is analogous to Equation S4, in which its maximum value is 1 when: $A_{rad} + A_{nrad}(T) \approx A_{nrad}(T)$. Therefore, the maximum temperature where S_0 can be achieved, in which we will call T_{+S_0} can be defined as:

$$T_{+S_0} < \sqrt{\frac{\Delta E}{k_B S_0}} \tag{S20}$$

This equation represents the high limit boundary, or in other words, the maximum temperature to achieve the given nominal sensitivity S_0. For example, if we are interested in sensitivity higher than 2% K^{-1}, we can use S_0 = 0.02 K^{-1}, leading to $T_{\geq S_0} = 10\sqrt{\Delta E/2k_B}$. Adopting $\Delta E(1)$ = 4500 cm^{-1} and $\Delta E(2)$ = 3500 cm^{-1}, we obtain: $T_{\geq 1.5}(1)$ = 570 K and $T_{\geq 1.5}(2)$ = 500 K. Therefore, only below this threshold temperatures can the thermometers achieve S_r = 2% K^{-1}. This shows that for two distinct thermometers to reach the same value S_0, the one with the lowest energy barrier will grasp sensitivity at lower temperature than its counterpart. This is the case with the PMMA:1% film compared to the freestanding complex. It should be noticed that this analysis relies solely on the energetic barrier, thereby providing a qualitative aspect of the temperature range rather than a quantitative one, as the interplay of the non-radiative rates will also help to shift the thermometer operational range.

(*ii*) Maximum relative sensitivity

To define the optimum temperature for the maximum relative sensitivity, first we can impose a stationary condition defined in Equation S21.

$$\frac{d}{dT}S_r(T)\Big|_{T=T_m}=0 \qquad \text{(S21)}$$

After this, we can abbreviate the parameters in Equation 3 of the main text by means of Equation S22 and rearrange S$_r$(T):

$$r=\frac{g_1A_{nrad}(0)}{A_{rad}},\ x=\frac{\Delta E}{k_BT} \qquad \text{(S22)}$$

$$S_r(T)=\frac{k_BT}{\Delta E}x^2\frac{re^{-x}}{1+re^{-x}} \qquad \text{(S23)}$$

Since *x* possesses a reciprocal relation with *T*, maximizing S$_r$(T) is equivalent to maximizing it with relation to *x*, enabling to proceed with: dS_r/dx = 0, generating equation S24, and its closed form – Equation S25.

$$x_m=2\left(1+re^{-x_m}\right) \qquad \text{(S24)}$$

$$\frac{\Delta E}{k_BT_m}=2\left[1+\frac{g_1A_{nrad}(0)}{A_{rad}}e^{-\Delta E/(k_BT_m)}\right] \qquad \text{(S25)}$$

To solve this equation, in other words, to isolate T_m is possible to use the lambert-W form. First, we let $u=x-2$, leading to $ue^u=2re^{-2}$. Following Lambert W relation: $W(z)e^{W(z)}=z$, we obtain Equation S26, which can be expanded to Equation S27 by using the identities settled in Equation S22.

$$u=W\left(2re^{-2}\right)\Rightarrow x_m=2+W\left(2re^{-2}\right) \qquad \text{(S26)}$$

$$T_m=\frac{\Delta E}{k_B\left[2+W\left(2e^{-2}\frac{g_1A_{nrad}(0)}{A_{rad}}\right)\right]} \qquad \text{(S27)}$$

It should be noted that in this case, *W* is the mathematical operator that converts the balance of intrinsic non-radiative and radiative rates into the corrected peak position T_m. In this sense, it is not a physical parameter, but a special function needed to solve the competition of processes. After finding the equation for T_m, we can return to the relative sensitivity to define S_m.

At S_m the stationary condition defined in Equation S21 can be written in terms of *r* and *x*, in the form of Equation S28.

$$re^{-x_m} = \frac{x_m}{2} - 1 \Rightarrow \frac{re^{-x_m}}{1 + re^{-x_m}} = \frac{x_m - 2}{x_m} \tag{S28}$$

By returning to Equation S23 and using the relation defined in Equation S28, we obtain Equation S29:

$$S_m = \frac{k_B}{\Delta E} x_m^2 \frac{x_m - 2}{x_m} = \frac{k_B}{\Delta E} x_m (x_m - 2) \tag{S29}$$

With this equation we can go back to the Lambert *W* relation defined before by substituting $x_m = 2 + W(2re^{-2})$, leading to Equation S30 and its expanded form Equation S31.

$$S_m = \frac{k_B}{\Delta E}\left(2 + W(2re^{-2})\right)W(2re^{-2}) \tag{S30}$$

$$S_m = \frac{k_B}{\Delta E}\left(2 + W\left(2\frac{g_1 A_{nrad}(0)}{A_{rad}}e^{-2}\right)\right)W\left(2\frac{g_1 A_{nrad}(0)}{A_{rad}}e^{-2}\right) \tag{S31}$$

From Equation 31 it is noteworthy that the maximum sensitivity can be achieved through (*i*) decreasing the activation energy and (*ii*) increasing $A_{nrad}(0)$. However, both dependences are non-linear because of the reciprocal reliance and the competition between non-radiative and radiative rates, respectively, which can lead to smaller maximum sensitivities even with lower individual parameters. Such findings were observed for the PMMA:1% film, which presented higher non-radiative decay combined with lower energy barrier, but with inferior maximum sensitivity due to this interplay. Thus, such outcomes offer a viable route to understanding how the dispersion of these complexes can tune the thermometric features to shift the optimal temperature range without compromising thermal response.

To solve equation S31, the Lambert W parameter should be solved. This parameter obeys the relation $W(x)e^{W(x)} = x$. By using the parameters of the film in Table 2, we obtain:

$r = \frac{g_1 A_{nrad}(0)}{A_{rad}} = 1.849 \times 10^6, \ \ x \ = 2re^{-2} = 5.006 \times 10^5$

$W(5.006 \times 10^5)e^{W(5.006 \times 10^5)} = 5.006 \times 10^5$

By taking $f = W(5.006 \times 10^5)$:

$fe^f = 5.006 \times 10^5 \Rightarrow \ln f + f = 13.1235$

By solving this equation, which can be done by either trial-and-error, numerical optimization or asymptotic estimate, we obtain *f* = 10.749, i.e., $W(2re^{-2}) =$ 10.749, which can be plugged into Equation S31. This also highlights the reason for the non-linear dependence of S_m with the balance of non-radiative and radiative rates.

Supplementary references

---

[1] A. C. F. Beltrame, A. G. Bispo-Jr, F. S. M. Canisares, R. V. Fernandes, E. Laureto, S. A. M. Lima, A. M. Pires, *Soft Matter* 2023, **19**, 3992.

[2] G. M. Sheldrick, *Acta Cryst.,* **2015**, C71, 3-8.

[3] R. T. Moura Jr, M. Quintano, C. V. Santos Jr, V. A. C. A. Albuquerque, E. C. Aguiar, E. Kraka, A. N. C. Neto, *Opt. Mat* 2022, **16**, 100216.

[4] Y. Ma, H. Wang, W. Liu, Q. Wang, J. Xu, Y. Tang, *J. Chem. Phys. B* 2009, **113**, 14139.

[5] C. Kodaira, H. F. Brito, O. L.Malta, O. A. Serra, *J. Lumin. 2003*, **101**, 11.

[6] C. D. S. Brites, A. Millán, L. D. Carlos, Lanthanides in Luminescent Thermometry. In: Handbook on the physics and chemistry of rare earths. *Elsevier* 2016, **49**, 339-427.

[7] F. Neese, *Wiley Interdiscip. Rev. Comput. Mol. Sci.* 2025, **15**, e70019.

[8] F. Neese, *Faraday Discuss.* 2024, **254**, 295.

[9] C. Adamo, M. Cossi, V. Barone, *J. Mol. Struct. THEOCHEM.* 1999, *493*,145.

[10] E. Caldeweyher, J-M. Mewes, S. Ehlert, S. Grimme, *Phys. Chem. Chem. Phys.* 2020, **22**, 8499.

[11] F. Weigend, *Phys. Chem. Chem. Phys.* 2005, **7**, 3297.

[12] J. Yang, S. Falletta, A. Pasquarello, *npj Comput Mater* 2023, **9**, 108.

[13] M. Dolg, H. Stoll, A. Savin, H. *Theoret. Chim. Acta* 1989, *75*, 173.

[14] M. Dolg, H. Stoll, H. Preuss, *Theoret. Chim. Acta* 1993, **85**, 441.

[15] F. J. Caixeta, L. F. Saraiva, B. D. Freitas, B. S. D. Onishi, S. H. Santagneli, R. Bortoletto-Santos, A. M. Pires, S. J. L. Ribeiro, *Chem. Asian J.* 2025, **20**, e202401612.

---

[16] O.L Malta, *J. Lumin.* 1997, **71**, 229.

[17] O. L. Malta, F. R. Gonçalves e Silva, *Spectrochim. Acta A Mol. Biomol. Spectrosc.* 1998, **54**, 1593.

[18] R. Longo, F. R. Gonçalves e Silva, O. L. Malta, *Chem. Phys. Lett.* 2000, **328**, 67.

[19] R. T. Moura Jr., Mateus Quintano, Carlos V. Santos-Jr, Vinícius A.C.A. Albuquerque, Eduardo C. Aguiar, Elfi Kraka, Albano N. Carneiro Neto, *Opt. Mater.:X* 2022, **16**, 100216.

[20] T. Kushida, *J. Phys. Soc. Jpn.* 1973, **34**, 1318.

[21] W. T. Carnall, H. Crosswhite, H. M. Crosswhite, Energy level structure and transition probabilities in the spectra of the trivalent lanthanides in LaF_3. Report of the Argonne National Laboratory, Argonne, Ill., U.S.A (1977). https://doi.org/10.2172/6417825

[22] A. N. Carneiro Neto, E. E. S. Teotonio, G. F. de Sá, H. F. Brito, J. Legendziewicz, L. D. Carlos, M. C. F. C. Felinto, P. Gawryszewska, R. T. Moura Jr., R. L. Longo, W. M. Faustino, O. L. Malta, In. Handbook on the Physics and Chemistry of Rare Earths, *Elsevier*, 2019, **56**, 55 – 162.

[23] S. Edvardsson, M. Klintenberg, *J. Alloys Compd.* 1998, **275–277**, 230.

[24] A. N. Carneiro Neto, R. T. Moura Jr, *Chem. Phys. Lett.* 2020, **757**, 137884.

[25] Riseberg, L. A., Moos, H. W., Multiphonon Orbit-Lattice Relaxation of Excited States for Rare Earth Ions in Crystals. *Phys. Rev.* 1968, 174, 429.

[26] H. W. Moos *J. Lumin.* 1970, **1 – 2**, 106.

[27] L. A. Riseberg, M. J. Weber, III *Progress in Opt*. 1977, **14**, 89.

[28] M. Suta, A. Meijerink, *Adv. Theory Simul.* 2020, **3**, 2000176.

[29] M. Pinsky, D. Avnir, *Inorg. Chem.*, **1998**, 37, 5575.

[30] Cameron F. Holder, Raymond E. Schaak, ACS Nano **2019**, 13, 7359−7365.